ORIGINAL RESEARCH ARTICLE

Electrically Heated Fluidized Bed for Graphite Purification: Heat Transfer and Electric Resistivity Models for Scale-Up

IMTIAZ AHMED, SERHII FEDOROV, ARTEM SYBIR, SEMEN HUBYNSKYI, and MARC DUCHESNE

Electrothermal purification is an effective method for achieving over 99.9 pct purity for graphite particles with minimal environmental impact. However, the lack of a suitable heat and electric resistivity model has hindered the scaling up of electrically heated fluidized bed (EHFB) reactors for graphite purification. In this study, three commercial natural graphite flake populations were tested in a bench-scale fluidized bed reactor at temperatures of up to 1000 °C. The experiments varied key parameters, including the graphite particle size, particle bed temperature, fluidization index, and electrode depth within the particle bed. Controlling the fluidized bed reactor at high temperatures requires an understanding of bed resistivity and how current flows throughout the EHFB system. The results show that fluidized bed resistivity decreases with temperature, with a diminished effect at higher temperatures. Smaller particles exhibit a higher resistance, likely due to a larger number of contact points required to pass current between the electrodes. In this study, a Finite Difference Method (FDM) model was developed using Visual Basic for Applications (VBA) in Excel®. Additionally, a Finite Element Method (FEM) model was created using COMSOL Multiphysics®. The FDM model assumes the current flows only radially, whereas the FEM model accounts for both radial and vertical current flow. The FDM model was validated against experimental data. Additionally, the FDM model was verified through a comparison with the FEM model. The FDM model showed good agreement with experimental resistance data and moderate agreement with power consumption, while the FEM model provided more accurate predictions by accounting for a detailed geometry and heat loss mechanisms. Achieving a uniform temperature distribution within the fluidized bed is influenced by the electrode's contact area. Deeper immersion of the electrode enhances thermal uniformity and provides results that more closely match experimental observations.

https://doi.org/10.1007/s11663-025-03758-7

I. INTRODUCTION

THE projected market growth for battery grade graphite is ~ 500 pct from 2023 to 2050.[1,2] A major supply chain bottleneck is purifying graphite to over 99.9 pct.[3,4] High-purity graphite also finds applications in electric arc furnaces, the nuclear industry, and electrocatalysis.[3] Natural graphite is mined and can be concentrated via physical purification stages to achieve a carbon content of up to ~ 95 pct.[5–7] For further purification of natural graphite, there are some common methods, which use chemical treatment, thermal treatment or the combination of both. Electrothermal treatment is a thermal process that uses electricity while avoiding the use of harsh chemicals.[8–10] Electrothermal treatment usually involves ultra-high temperature (~ 3000 °C) purification and is currently mostly applied for synthetic graphite purification, as opposed to natural graphite purification.[11–13]

One commercial technology for electrothermal treatment is the Acheson furnace.[14] However, there are some scale-up and operational challenges with this furnace type, such as its high energy requirements due to elevated heat losses, limited feedstock versatility, non-continuous operation, low capacity per batch, and extended downtime. Alternatively, an electrothermal fluidized bed furnace allows for both batch and continuous processing of granular carbon matter up to 3000

IMTIAZ AHMED and MARC DUCHESNE are with the Natural Resources Canada, CanmetENERGY in Ottawa, Ottawa, ON K1A 1M1, Canada. Contact e-mail: imtiaz.ahmed@nrcan-rncan.gc.ca SERHII FEDOROV, ARTEM SYBIR, and SEMEN HUBYNSKYI are with the Thermal & Material Engineering Center SP. Z O. O., 45-0477 Opole, Poland.

Manuscript submitted March 21, 2025; accepted August 12, 2025.

Published online: 21 October 2025

°C. Other major advantages of using an electrothermal fluidized bed include (a) uniform product properties, (b) control of the graphitization degree, (c) high energy efficiency, and (d) feedstock flexibility (*e.g.*, natural and synthetic origin, recycled waste carbon).[8,15] However, predicting the performance and operational characteristics of such reactors remains a significant challenge. The lack of suitable and robust models continues to hinder the upscaling of this technology. This study addresses this critical gap by introducing a novel model that integrates heat transfer and electric resistivity model within such systems. The proposed model provides predictions for achievable temperatures, power consumption, and other key performance indicators, offering valuable insights to support the advancement of electrothermal fluidized beds.

Figure 1 is a typical configuration of an electrothermal fluidized bed using direct Joule heating. In this setup, the bed material must consist of electrically conductive substances, such as graphite, to enable the flow of electric current between the electrodes. This current passes through the bed inventory, causing the material to heat up due to its electrical resistance. Heat generation occurs either within individual particles or in the gas phase when electrical arcs form. The fluidized bed facilitates continuous particle circulation, ensuring a uniform temperature distribution throughout the bed.[15–17]

Achieving a certain temperature is dependent on the resistance of the fluidized bed. Therefore, this parameter plays a crucial role and must be modeled as a function of dominant factors, including temperature, bed material properties, fluidization index, particle size, particle shape, and the effects of bubble formation within the fluidized bed. Existing literature does not offer a comprehensive fluidized bed model including hydrodynamics combined with direct Joule heating. Although models were created for spherical coke particles in a fixed bed configuration,[18,19] there are challenges in accounting for fluidized bed hydrodynamics, particularly if considering non-spherical bed particles, such as natural graphite flakes.

This study presents experimental observations and analysis of three different graphite flake populations, *i.e.*, jumbo, large, and medium, along with the development of two heat transfer and electric resistivity models. The first model applies the Finite Difference Method (FDM) in Excel-VBA. The second model applies the Finite Element Method (FEM) in COMSOL Multiphysics®. The advantages and limitations of these models are discussed. These models provide valuable insights for optimizing reactor design and identifying scale-up scenarios, demonstrating their practical utility in reactor engineering and process optimization.

In this manuscript, Section II describes the graphite flakes used for the experimental investigation and modeling. The experimental setup is detailed in Section III. The FDM model is described in Section IV, while Section V outlines the FEM model. Section VI presents the experimental results, FDM model validation, and a comparison of the FDM and FEM models. Finally, Section VII concludes by summarizing the experimental and modeling activities and discussing the impact of the results on reactor design.

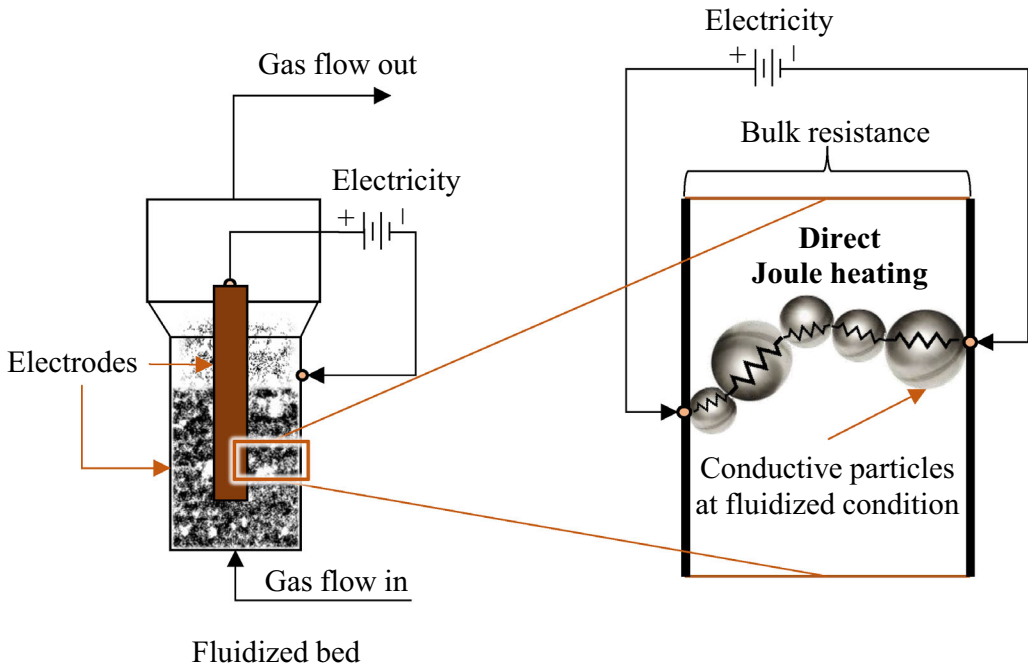

Fig. 1—A typical electrically heated fluidized bed for graphite purification.

II. MATERIALS

The electrothermal tests were performed on three natural graphite flake grades. The samples were provided by Nouveau Monde Graphite following a flotation process at their Saint-Michel-des-Saints production site in Quebec. The commercial names of the grades are jumbo (lot: 21-0205N0036), large (lot 21-0508N0084), and medium (lot 18-0815N0007). Table I presents the properties of these flakes.

III. EXPERIMENTAL SETUP

The electrothermal experiments were conducted in an electrically heated fluidized bed (EHFB) reactor designed to operate up to 1200 °C. Figure 2 is a photograph of the top of the reactor during one of the experiments. The reactor has a 110 mm inner diameter with a solid central electrode of 20 mm in diameter. The system includes a set of gas flowmeters (0 to 50 L/min: accuracy ± 2.5 pct of the full scale), a power supply system (0 to 100 V, 5 kW: accuracy ± 3.5 pct), and a thermocouple (type K: 0 °C to 1200 °C: accuracy ± 2.5 pct of the full scale). Both the center electrode and the reactor, which also acts as an electrode, are made of graphite. The top section is made of borosilicate glass for visual observation of the process. The thermocouple is aligned with the bottom edge of the central electrode. The gas distributor was formed by a layer of ceramic beads with a height of 60 mm, each bead having a diameter of 1 to 3 mm. Argon was used for fluidization. Prior to fluidization, the graphite bed height was ~ 130 mm for all experiments. The system allows to change the immersion depth of the central electrode from 25 to 95 mm.

W_{mf_a} is the ratio of the active zone superficial gas velocity to the minimum fluidization velocity (u_{mf}). The experiments were conducted with a W_{mf_a} within the range of 1 to 5. The depth of the central electrode inside the graphite bed was varied from 25 to 95 mm. In a prior study, beds formed by jumbo flakes demonstrated gas bubble formation along with an intensive mixing of bed particles, which represents Geldart group B particle characteristics. The large and medium flakes showed Geldart group C behavior.[20] Measurements reported in this study were recorded after 3 to 5 minutes of stable operation at each condition. All the experimental data points are assumed to be at steady state, based on the observation of a constant fluidized bed temperature.

Previous experiments revealed that a complete fluidization occurs while the W_{mf_a} is greater than 1.1 for jumbo, 1.7 for large, and 3 for medium particles.[20] Hence, the u_{mf} is not always equal to the complete fluidization velocity, denoted as u_{cf}. Furthermore, the fluidization index in the bottom zone (see Figure 3) will differ from the fluidization index in the active zone due to the cross-sectional area change along the flow of fluidizing gas. Hence, the active zone complete fluidization index is defined as $W_{cf\_a,}$ which is a ratio of the active zone superficial gas velocity to u_{cf}. Similarly, W_{cf_b} is the bottom zone complete fluidization index, *i.e.*, a ratio of the bottom zone superficial gas velocity to u_{cf}. The u_{mf} and u_{cf} values of graphite flakes were determined experimentally at ambient temperature and pressure as listed in Table II.[20] In the present study, u_{cf} is calculated using the ratio of u_{cf}/u_{mf}, which is assumed to be independent of temperature.

IV. FDM MODEL

A. *Geometry*

A simplified two-dimensional geometry is considered to reduce the computational effort as presented in Figure 3. The FDM model is applied to the active zone in Figure 3. Assumptions about the boundary conditions rely on the characteristics of the full geometry in Figure 3. The actual outer shell is square, while the simplified geometry considers a cylindrical outer shell; it

Fig. 2—Photograph of the top of the EHFB during testing.

Table I. Properties of Natural Graphite Flakes

Properties/Samples Name	Jumbo	Large	Medium
Mass-Averaged Diameter from Sieving (μm)	338	215	123
Sauter Mean Diameter[20] (Fixed Bed Permeameter)	79	60	34
Bulk Tap Density[20] (kg/m^3)	770	830	758
Fixed Bed Resistivity[21] (4-Probe Method) (ohm cm)	4.7	8.6	10.8
Minimum Fluidization[20] Velocity (cm/s)	6.28	2.81	1.13

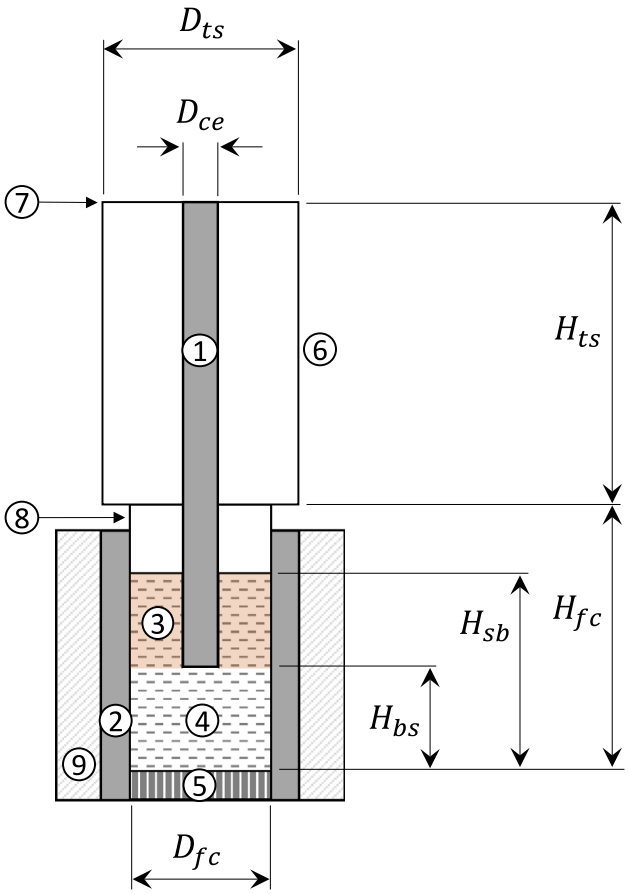

Fig. 3—Geometry for fluidized bed modeling. The geometry includes (1) a central electrode, (2) a side wall electrode, (3) an active zone of the fluidized bed, (4) a bottom zone of the fluidized bed, (5) a gas distributor, (6) borosilicate glass shell, (7) a top steel cover, (8) a steel shell, and (9) insulation.

Table II. Ratio of u_{mf} and u_{cf}

	Jumbo	Large	Medium
u_{mf}	0.063	0.028	0.011
u_{cf}	0.070	0.046	0.035
u_{cf}/u_{mf}	1.11	1.64	3.10

is assumed that the change has a negligible effect on heat transfer. Table III lists the dimensions considered for the model evaluation.

B. *Model Development*

1. *Fluidization*

It is assumed that the parameters of the FB, *i.e.*, gas flow rate, void fraction of the emulsion phase, and bubble fraction, are uniformly distributed across the FB. The minimum fluidization velocity can be calculated, while the process temperature, pressure, particle characteristic dimension, and fluidizing medium are known. It is assumed that the ideal gas law is valid for the experimental conditions encountered in this study.

Equation [1] can be used to obtain the Archimedes number (Ar), where d_p is the characteristic particle diameter, ρ_m is the density of the fluidized material, ρ_g is the density of the fluidizing medium, g is the standard acceleration due to gravity, and v is the kinematic viscosity of the gas media. Equation [2] can be used to calculate the Reynolds number at minimum fluidization (Re_{mf}).[22]

$$Ar = \frac{g \cdot d_p^3}{v^2} \cdot \frac{(\rho_m - \rho_g)}{\rho_m}, \quad [1]$$

$$Re_{mf} = \frac{Ar}{1400 + 5.22 \cdot \sqrt{Ar}}, \quad [2]$$

$$u_{mf} = \frac{Re \cdot v}{d_p}. \quad [3]$$

Equation [3] expresses the u_{mf}, where v can be evaluated using Eq. [4], μ is the dynamic viscosity of the fluidizing gas and can be evaluated by Eq. [5], and ρ_g is the gas density that can be evaluated by Eq. [6] as a function of temperature (T) and pressure (P). All the parameters at standard conditions are denoted by a subscript zero, *i.e.*, $T_0 = 293\text{K}$ and $P_0 = 101{,}325\text{Pa}$. Equation [5] allows the calculation of μ as a function of temperature, where C is the Sutherland constant,[23] and μ_0 is the dynamic viscosity at standard conditions.[24] The following constants were used to evaluate μ : $C_{N2} = 104.7$ K, $C_{Ar} = 146.3$ K,[25] $\mu_{0_{N2}} = 1.66 \times 10^{-5}\text{Pa} \cdot \text{s}$, $\mu_{0_{Ar}} = 2.1 \times 10^{-5}\text{Pa} \cdot \text{s}$,[24] and $\rho_{0_{N2}} = 1.25 \frac{\text{kg}}{\text{m}^3}$, $\rho_{0_{Ar}} = 1.78 \frac{\text{kg}}{\text{m}^3}$.

$$v = \frac{\mu}{\rho_g}, \quad [4]$$

$$\mu = \mu_0 \cdot \frac{(273 + C)}{(T + C)} \cdot \left(\frac{T}{273}\right)^{\frac{3}{2}}, \quad [5]$$

$$\rho_g = \rho_{g0} \cdot \frac{P}{P_0} \cdot \frac{T_0}{T}. \quad [6]$$

The void fraction (ε) of the FB is expressed in Eq. [7].[26] Equation [8] defines bubble fraction (φ_b), where V_{bubble} is the volume of bubbles in the fluidized bed, V_{fb} is the volume of the fluidized bed, and ε_{mf} is the void fraction at the minimum fluidization condition.

Table III. System Dimension

Symbols	Description	Value (mm)
D_{CE}	diameter of the central electrode (CE)	20
D_{ts}	inner diameter of the top space	144
D_{fc}	inner diameter of the side wall electrode (SWE)	110
H_{bs}	bed height beneath the CE	35 to 105
H_{sb}	bed height prior to fluidization	130
H_{fc}	fluidization chamber height	270
H_{ts}	height of the top space	200

$$\varepsilon = \varepsilon_{mf} \cdot \left(\frac{Re_{mf} \cdot Wmf_a + 0.02 \cdot (Re_{mf} \cdot Wmf_a)^2}{Re_{mf} + 0.02 \cdot Re_{mf}^2} \right)^{0.1}, \quad [7]$$

$$\varphi_b = \frac{V_{bubble}}{V_{fb}} = \frac{\varepsilon - \varepsilon_{mf}}{1 - \varepsilon_{mf}}. \quad [8]$$

2. *Heat transfer*

The heat losses from the system occur radially, upward and downward. These losses are assumed to be uniformly distributed across the corresponding areas. Within the EHFB, heat transfer primarily results from intensive material mixing, while radiative heat transfer is minimal due to the dense structure of the fluidized bed.[26,27] Equation [9] describes the steady-state temperature field inside the active zone of the FB[26,27]:

$$\frac{\lambda_{ef}(r,z)}{\rho_m \cdot (1-\varepsilon) \cdot c_m} \cdot \left(\frac{\partial^2 T}{\partial r^2} + \frac{1}{r} \cdot \frac{\partial T}{\partial r} + \frac{\partial^2 T}{\partial z^2} \right) + \frac{q_v(r,z)}{\rho_m \cdot (1-\varepsilon) \cdot c_m} = 0, \quad [9]$$

where $\lambda_{ef}(r,z)$ is the effective thermal conductivity of the FB, $q_v(r,z)$ is the specific Joule heating rate inside the FB, ρ_m is the density of the fluidized material, c_m is the specific heat capacity of the fluidized material, and T is the local temperature of the FB. The radial and vertical coordinates are noted as r and z, respectively. Table IV is a list of boundary conditions for Eq. [9].

The value of $\lambda_{ef}(r,z)$ of a FB depends on material mixing. Equations [10] through [13] are the correlations addressing material mixing intensity to calculate $\lambda_{ef}(r,z)$ based on experimental data from literature.[26]

$$\lambda_{ef}(r,z) = a_{ef}(r,z) \cdot \rho_m \cdot (1-\varepsilon) \cdot c_m, \quad [10]$$

$$a_{ef.r} = 1.4 \cdot v \cdot (Wmf_a - 1)^{0.35} \cdot Ar^{0.12} \cdot \left(\frac{H_{AZ}}{D_{AZ}} \right)^{0.05}, \quad [11]$$

$$a_{ef.z} = 2.74 \cdot v \cdot (1-\varepsilon)^{-1} \cdot (Wmf_a - 1)^{0.54} \cdot Ar^{0.144} \cdot \left(\frac{H_{AZ}}{D_{AZ}} \right)^{1.3}, \quad [12]$$

$$D_{AZ} = D_{fc} - D_{CE}, \quad [13]$$

where $a_{ef.r}$ and $a_{ef.z}$ are apparent thermal diffusion coefficients of the FB in the radial and vertical directions, respectively.

3. *Current flow*

The electric current passes from the positive CE to the negative SWE in the radial direction within the volume of the active zone. The active zone of the FB is considered as multiple horizontal layers. It is assumed that each layer is electrically isolated from the others. Therefore, the electric current for each horizontal layer "i" can be determined with the following equation:

$$I_i = \frac{\Delta U_i}{\sum R_j}, \quad [14]$$

where ΔU_i is the voltage drop between the CE and the SWE within a single horizontal layer "i" of the FB and $\sum R_j$ is the overall resistance of a single horizontal layer of the FB calculated as a sum of the resistances in the radial direction. Table V is a list of boundary conditions to evaluate ΔU_i for Eq. [14].

The total current value is calculated as the sum of electric currents through each horizontal layer:

$$I_\Sigma = \sum I_i. \quad [15]$$

The overall voltage drop in the reactor is determined as follows:

$$\Delta U = U_{i=0} - U_{r=\frac{D_{fc}}{2}}. \quad [16]$$

4. *Resistivity*

The following assumptions are made while developing the resistivity model: (a) the main volume responsible for Joule heating of the FB is limited by the active zone and located between the CE and SWE, (b) the electric contact between the bottom side of the CE with the FB is negligible, (c) the electrical current passes through the horizontal layers of the FB between the CE and SWE, and (d) the electrical resistance at the interfaces between the electrodes and the FB is neglected.

The electrical resistivity is based on the concept of resistivity of a single contact between two particles. This approach considers the influence of particle size, particle shape, and structure of the FB. The resistivity of an element volume ($\Omega_{i,j}$) can be determined as follows[28–30]:

$$\Omega_{i,j} = K \cdot \frac{d_\mathrm{p}}{0.99 - 1.34 \cdot \varphi_\mathrm{b}} \cdot R_{\mathrm{c}\Sigma i,j}, \qquad [17]$$

where K is the structure coefficient accounting for the influence of broken contacts between particles in the bed. For a fixed bed, $K = 1$, while for the emulsion phase of a fluidized bed, $K = 7$ to 9.[28] In this study, $K = 2$ for medium graphite flakes, 3 for large graphite flakes, and 4 for jumbo graphite flakes. $R_{\mathrm{c}\Sigma i,j}$ is the resistance of a contacting pair of particles. The denominator, $0.99 - 1.34 \cdot \varphi_\mathrm{b}$, is based on simulations performed for porous structures.[29]

The resistance of a contacting pair of particles, $R_{\mathrm{c}\Sigma}$ (Figure 4), is calculated by summing up the contact resistance, R_c, and particle resistance, R_p.

$$R_{\mathrm{c}\Sigma} = R_\mathrm{c} + R_\mathrm{p}. \qquad [18]$$

The resistance of the contact area depends on the current density and the temperature. Equation [19] for R_c is obtained on the basis of the experimental data for synthetic graphite particles of 127 μm by Borodulya.[31,32] C_q is the heat coefficient expressed in Eq. [20] where $Q_{\mathrm{eli,j}}$ is the heat released in the element (i,j) of the FB and $V_{\mathrm{eli,j}}$ is the volume of the element (i,j).

$$R_\mathrm{c} = -69.93 - 9.87 \cdot C_\mathrm{q} + \frac{6.58 \cdot 10^5}{T} - 637.64 \cdot \frac{C_\mathrm{q}}{T} - \frac{1.28 \cdot 10^8}{T^2} + 0.096 \cdot C_\mathrm{q}^2, \qquad [19]$$

$$C_\mathrm{q} = \frac{Q_{\mathrm{eli,j}}}{V_{\mathrm{eli,j}}} \cdot \frac{1}{1 - \varphi_\mathrm{b}}, \mathrm{W/cm^3}. \qquad [20]$$

Equation [21] provides the corrected contact resistance, $R_\mathrm{c}\prime$, which accounts for the dependency of particle size,[28] where d_p is the diameter of particles in μm; $\alpha \approx 0.5$ is an experimental coefficient. The numerical value 127 μm in Eq. [21] refers to the diameter of particles studied by Borodulya,[31] and the d_p is expressed in μm.

$$R_\mathrm{c}\prime = R_\mathrm{c} \cdot \left(\frac{127}{d_p}\right)^{\alpha+1}. \qquad [21]$$

The electrical resistance of a single particle, R_p, is calculated using the average distance between neighboring particle centers, l_p, and the average cross-sectional area of a particle, F_p. l_p, and F_p were determined based on the assumptions that the void fraction of the emulsion phase of the FB is the same as at the minimum fluidization condition; the values were calculated considering the known number of particles inside a single-volume element.

$$R_\mathrm{p} = \Omega_\mathrm{m} \cdot \frac{l_\mathrm{p}}{F_\mathrm{p}}. \qquad [22]$$

The variables l_p and F_p are expressed mathematically in Eq. [23] assuming cylindrical particles (flakes), where s_p is the height of a particles (thickness of a flake). Equation [24] represents spherical particles.

$$\text{For flakes, } l_\mathrm{p} = \left(\frac{\frac{\pi}{4} \cdot d_\mathrm{p}^2 \cdot s_\mathrm{p}}{1 - \varepsilon_\mathrm{mf}}\right)^{1/3}; F_\mathrm{p} = \frac{\left(\frac{\pi}{4} \cdot d_\mathrm{p}^2 \cdot s_\mathrm{p}\right)^{2/3}}{(1 - \varepsilon_\mathrm{mf})^{1/3}}, \qquad [23]$$

$$\text{For spheres, } l_\mathrm{p} = d_\mathrm{p} \cdot \left(\frac{\pi}{6 \cdot (1 - \varepsilon_\mathrm{mf})}\right)^{\frac{1}{3}}; F_\mathrm{p} = d_\mathrm{p}^2 \cdot (1 - \varepsilon_\mathrm{mf})^{\frac{1}{3}} \cdot \left(\frac{\pi}{6}\right)^{\frac{2}{3}}. \qquad [24]$$

$R_{i,j}$ is the horizontal resistance of a single-volume element for the current passing from the CE to the SWE:

$$R_{i,j} = \Omega_{i,j} \cdot \frac{1}{2 \cdot \pi \cdot \Delta z} \cdot \ln \frac{r_j + \frac{\Delta r}{2}}{r_j - \frac{\Delta r}{2}}, \qquad [25]$$

$$Q_{\mathrm{eli,j}} = I_i^2 \cdot R_{i,j}, \qquad [26]$$

$$I_i = \frac{\Delta U_i}{\sum R_{i,j}}. \qquad [27]$$

Equations [25] through [27] close the system of Eqs. [19] through [24]. The average electrical resistivity (Ω) of the active zone is expressed as Eq. [28] where H_AZ is the height of the active zone.

$$\Omega = \frac{\Delta U}{I_\Sigma} \cdot \frac{2 \cdot \pi \cdot H_\mathrm{AZ}}{\ln \frac{D_\mathrm{fc}}{D_\mathrm{CE}}}. \qquad [28]$$

5. *Numerical approach*

The numerical evaluation of the FDM model is performed using Excel®-VBA. The model calculates the active zone parameters and considers the heat losses to the ambient environment. Figure 5 is the schematic diagram of the grid as applied in the numerical

Table IV. Boundary Conditions for Heat Transfer Calculations

Boundary Description	Boundary Conditions
Neumann Boundary Condition—No Heat Flux at the Outer Surface of CE	$\lambda_{\text{ef.r}} \cdot \frac{\partial T}{\partial r}\Big\vert_{r=\frac{D_{\text{ce}}}{2}} = 0$
Heat Loss on the Surface of the SWE	$\lambda_{\text{ef.r}} \cdot \frac{\partial T}{\partial r}\Big\vert_{r=\frac{D_{\text{fc}}}{2}} = q_{\text{SWE}}$
Heat Loss on the Top Surface of the FB	$\lambda_{\text{ef.z}} \cdot \frac{\partial T}{\partial z}\Big\vert_{z=0} = q_{\text{Top}} + q_{\text{G}} + q_{\text{ML}}$
Heat Loss at the Bottom Surface of the FB Active Zone	$\lambda_{\text{ef}} \cdot \frac{\partial T}{\partial h}\Big\vert_{z=H_{\text{AZ}}} = q_{\text{Bot}} + q_{\text{P}}$

Note $\boldsymbol{q_{\text{SWE}}}$ is the heat flux through the SWE which is equal to the heat loss through the insulation; q_{Top} is the heat flux through the top section of the reactor caused by radiation and thermal conductivity; q_{G} is the heat flux of effluent gases through the top section of the reactor; q_{ML} is the heat flux of the material carried over by the gases including evaporated impurities; q_{Bot} is the heat flux through the bottom section of the reactor caused by thermal conductivity; q_{P} is the heat flux with the material moving downwards to the discharge port; and $H_{\text{AZ}} = H_{\text{sb}} - H_{\text{bs}}$ is the height of the active zone..

Table V. Boundary Conditions for the Electric Domain

Boundary Description	Boundary Conditions
Voltage on the SWE Surfaces	$U_{r=\frac{D_{\text{fc}}}{2}} = 0$
Voltage on the CE Surfaces	$U_{r=\frac{D_{\text{ce}}}{2}} = U_i^*$
Voltage of the CE for the Neighboring Upper Layer	$\Delta U_{i-1} = \Delta U_i + \left(U_{i-1}^* - U_i^*\right)$

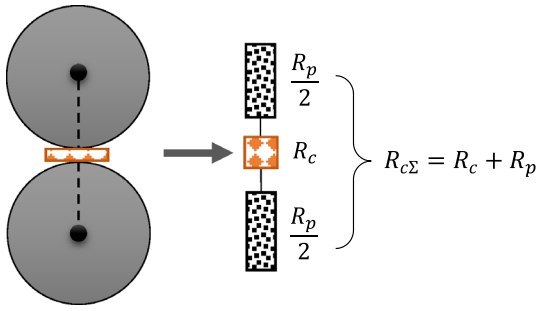

Fig. 4—Resistance model of inter-particle contact.

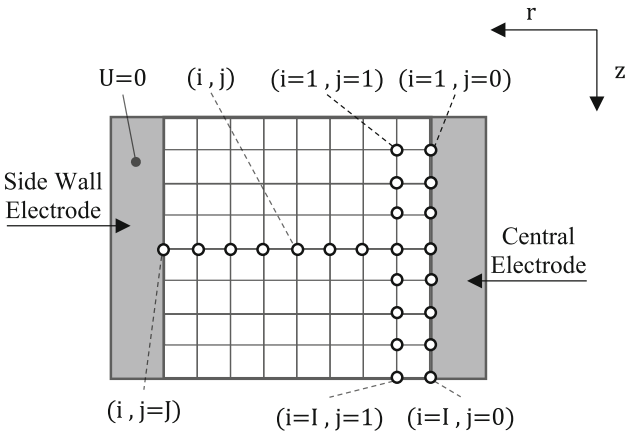

Fig. 5—Schematic diagram of the grid applied to an active zone half-symmetry.

calculation. The calculation is performed only to half of an active zone two-dimensional plane, as the active zone is radially symmetric.

To solve Eqs. [9] through [16], the FB was divided into elemental volumes with predefined steps in height and radius. Equation [9] is solved to generate the temperature field for each elemental volume of the FB. The system is solved based on a local one-dimensional finite difference scheme and the Gauss method. Figure 6 is the high-level algorithm of the numerical solver. The physical properties of materials, such as the electrical resistivity of graphite,[33] specific heat capacity of *Ar*,[34] and heat capacity and thermal conductivity of graphite,[35] are taken from literature.

V. FEM MODEL

A. *Numerical Approach*

The numerical evaluation with the FDM model is convenient and quick to estimate the active zone temperature profile, bed resistance, and power requirement to achieve a certain average bed temperature. Using a more refined geometry and predicting the temperature profile for the entire system (*i.e.*, reactor core, body, and insulation) would be challenging in Excel®-VBA. Therefore, COMSOL Multiphysics® 6.1 was used to address these challenges by FEM simulations. A desktop computer with Intel(R) Xeon(R) Gold 6258R CPU @ 2.70 GHz 2.69 GHz (2 processors), 256 GB RAM, and Windows 10 Enterprise, 64-bit, was employed.

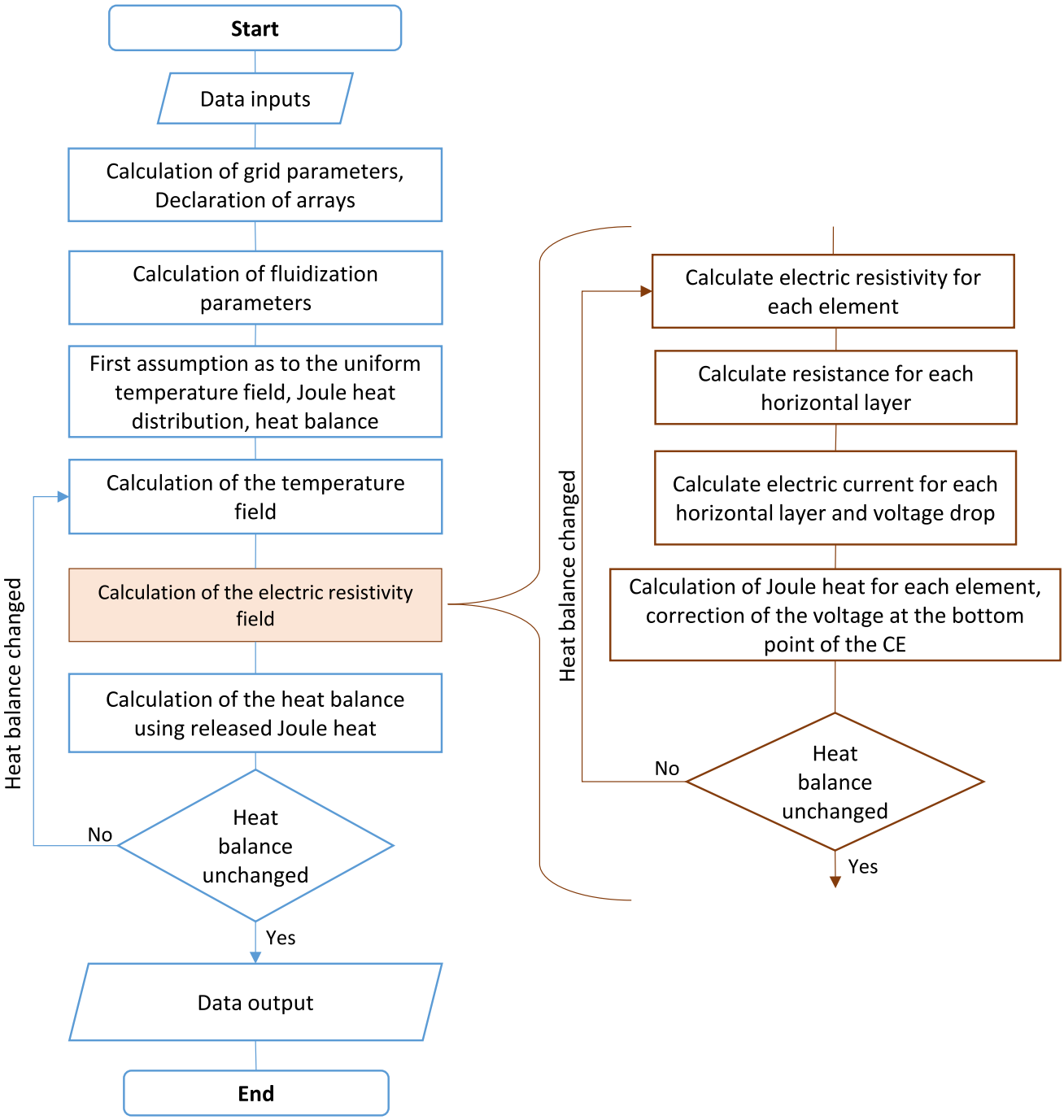

Fig. 6—Flow diagram for the FDM.

In this study, the *electromagnetics-AC/DC* and *heat transfer* modules were used. For the geometry and meshing, built-in tools were utilized. The objective was to conduct a stationary simulation to determine the steady-state temperature of the reactor system. As the temperature increased significantly relative to the initial conditions, convergence challenges arose for certain mesh configurations. These challenges were addressed by first solving the system at a lower temperature, controlled through a reduced voltage input as a boundary condition, then using the resulting solution as the initial value set for subsequent simulations at higher temperatures.

B. *Geometry and Boundary Conditions*

In the FEM model, a three-dimensional axisymmetric geometry of the bench-scale setup was represented by a half-plane two-dimensional model. This method greatly reduces computational time compared to using a full three-dimensional geometry. Boundary conditions for the model include (1) there is a constant positive

potential at the top of the central electrode, (2) the side wall electrode is a ground potential, (3) radiation can be transmitted to the environment from the top surface of the fluidized bed, (4) on the outer reactor surfaces, there is surface-to-ambient heat loss combined with natural convective heat loss or a constant wall temperature (for the sake of comparison with the FDM model, both conditions were analyzed), and (5) inner surfaces for void spaces have surface-to-surface radiation. The internal fluid medium is assumed stagnant, with convective heat loss considered negligible.

C. *Model Development*

The model employs the following physics interfaces: (a) Joule heating and (b) surface-to-surface radiation. A brief introduction of all interfaces is provided as follows. Further details on models are described in COMSOL documentation.[36]

1. *Joule heating interface*

The Joule heating interface is utilized in this study to model resistive heating based on Ohm's law. The simulation employs the direct current (DC) mode, where electric voltage is defined as an input parameter. This interface integrates the physics of electric currents and heat transfer in solid and fluid domains, enabling a coupled analysis of thermal and electrical effects. The temperature distribution is governed by a partial differential equation derived from Fourier's law, with contributions from heat sources such as electrical power dissipation.

In the simulations, both electric currents and heat transfer interfaces are used concurrently to account for electric power dissipation, which acts as a heat source within the system. The Joule heating interface facilitates the selection of fluid materials, enabling the simulation of convective and radiative heat transfer. The heat loss from the outer wall to the ambient environment accounts for natural convection and radiative heat transfer. In the case of radiation, the net heat flux due to surface-to-ambient radiation is calculated using the Stefan–Boltzmann equation.

The power dissipation for a given voltage is a function of the material's resistivity as indicated by Eqs. [19] and [20], which typically varies with temperature. In COMSOL, a custom function was implemented to incorporate these dependencies. Additional parameters affecting resistivity are discussed in Section IV–B–iv. Depending on the complexity of the problem, both stationary and time-dependent simulations were performed.

2. *Surface-to-surface radiation interface*

The surface-to-surface radiation interface models thermal radiation as an energy transfer between boundaries and external heat sources, assuming a transparent medium that does not participate in the radiation process. In this study, the high operational temperature required the inclusion of radiation heat transfer between surfaces. Radiation heat loss from the top of the FB surface occurs through a glass cover. Internal radiation absorption within the glass was neglected, and only surface radiation was considered.

3. *Assumptions and scope*

Material properties used in the simulations were either sourced from the COMSOL database or relied on custom functions based on material vendor or literature data. All material properties were consistent with those used in the FDM model.

The FEM model was designed to study heat generation and transfer rather than simulate particle and fluid dynamics in a fluidized bed. Heat generation occurs *via* Joule heating as current flows through the FB material against its electrical resistance. The FB was treated as a solid material; as such, the thermal conductivity and the electric resistivity of the FB were defined using Eqs. [10] and [17], respectively, to represent its electrothermal properties. The bed resistivity and thermal conductivity were modeled as a function of the fluidization index, particle size, temperature, and power dissipation. The internal fluid medium was treated as stagnant, hence heat loss due to fluid flow was not included in this simulation.

VI. RESULTS AND DISCUSSION

A. *Effect of Temperature*

The measured electrical resistance at different temperatures is presented in Figure 7 (for jumbo and large particles) and Figure 8 (for medium particles). In most cases, the fluidized bed resistance diminishes as the temperature increases. Note that graphite's intrinsic resistivity is known to decrease with an increase in temperature up to 1000 °C.[37,38] In the case of jumbo particles, the reduction of resistance with increasing temperature is prominent below 500 °C, while there is no significant change in resistance from 500 °C to 1000 °C. From 100 °C to 1000 °C, the resistance decreased by ~ 56 pct for jumbo particles; the resistivity of graphite only decreases by ~ 23 pct for the same temperature range.[37–39] This indicates that the change in graphite's intrinsic resistivity alone cannot explain the drop in resistance for the fluidized bed.

B. *Effect of the Fluidization Index*

The experimental resistance and the W_{cf_a} at different temperatures are presented in Figures 7 and 8. The results indicate that W_{cf_a} has little effect on resistance when particles are fully fluidized ($W_{cf\_a} > 1$). It was observed in another study that, at lower fluidization indices, bed resistance increases sharply with the fluidization index; however, this effect becomes less pronounced at higher fluidization indices.[39]

C. *Effect of Particle Grade*

Figure 9 illustrates the influence of particle grade on electrical resistance at 500 °C where the fluidization index was consistent ($W_{cf\_a} = 3.0 \pm 0.5$). Working with

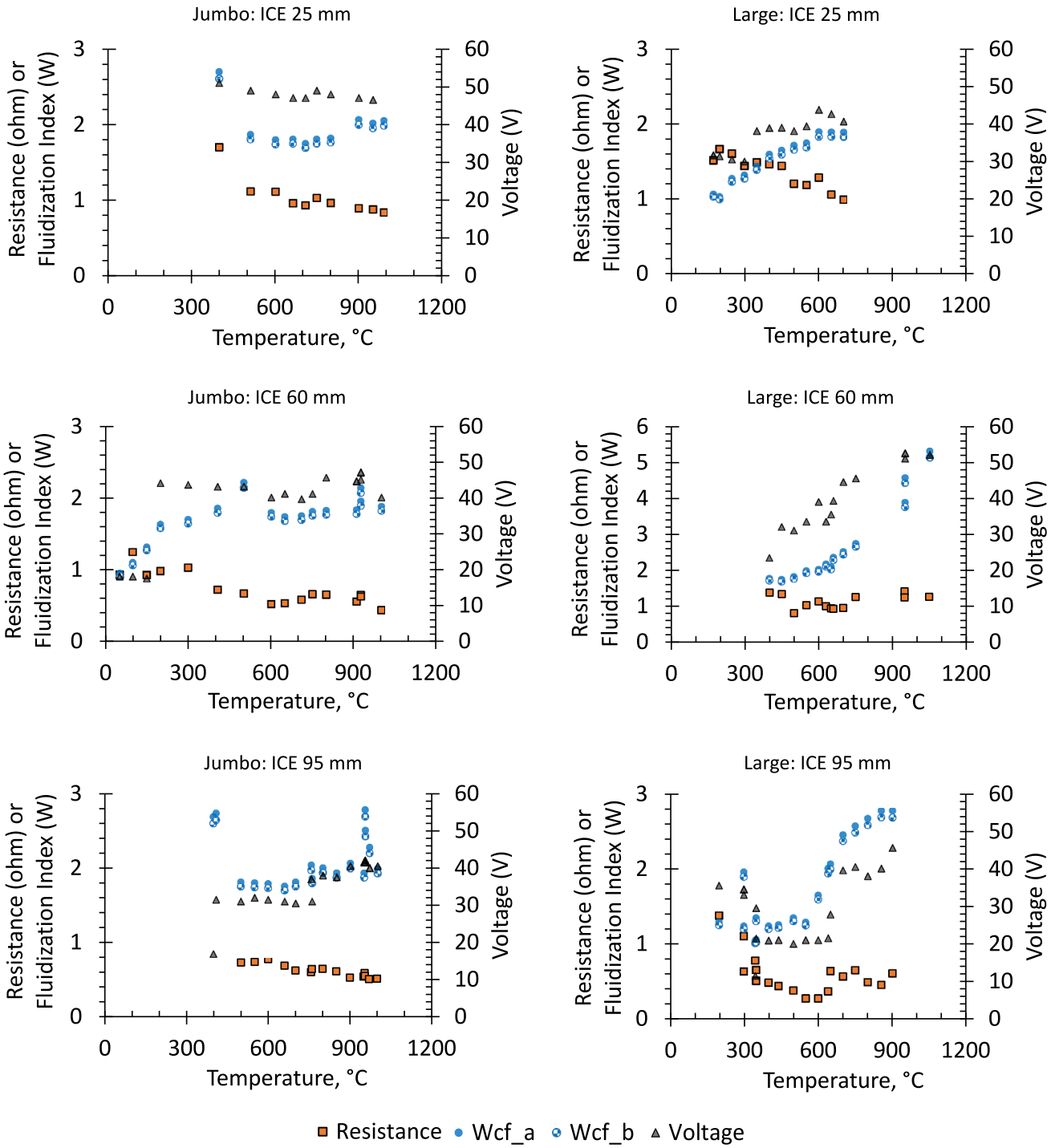

Fig. 7—Experimental resistance and fluidization index at different temperatures for jumbo and large particle grades. W_{cf_a} fluidization index for complete fluidization in the active zone and W_{cf_b} fluidization index for complete fluidization in the bottom zone.

medium particles was very challenging due to its poor fluidization; hence, data were only obtained for ICE 70 mm, while experiments with large and jumbo used an ICE of 60 mm. It is assumed that there is no significant hydrodynamic changes due to the 10 mm insertion difference. In Figure 9, *Resistivity-active zone* represents the resistivity of the active zone calculated from the resistance, assuming that current is only transmitted radially and within the active zone, *i.e.*, applying Eq. [28]. *Resistivity-actual geometry* represents the resistivity of the full bed, calculated from the resistance, by applying an FEM model using the reactor's inner geometry in COMSOL with the measured voltage drops and currents across the fluidized bed (represented by a uniform solid). The FEM model indicates that the actual volume through which current passes is larger

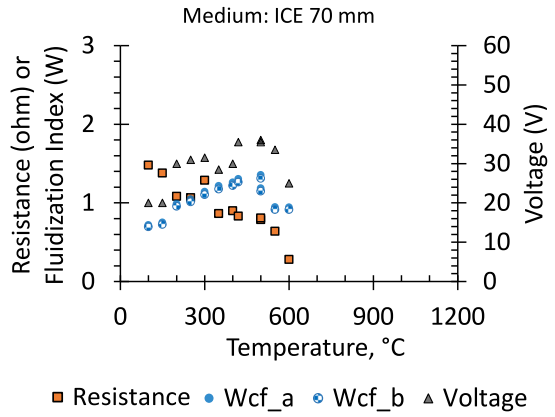

Fig. 8—Resistance and fluidization index at different temperatures for medium grade particles. W_{mf_a} fluidization index for minimum fluidization in the active zone, W_{cf_a} fluidization index for complete fluidization in the active zone, and W_{cf_b} fluidization index for complete fluidization in the bottom zone.

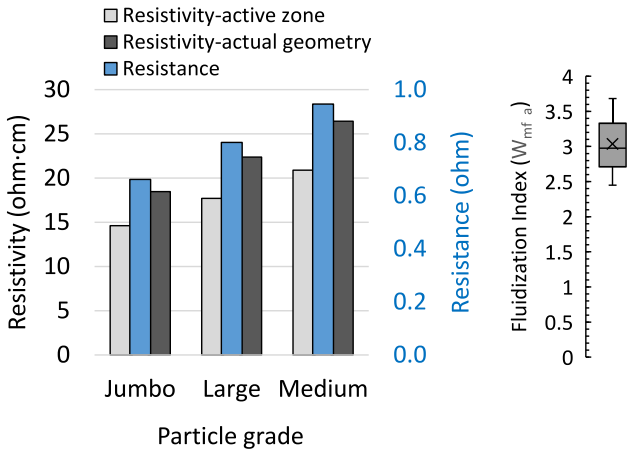

Fig. 9—Influence of particle grade on electrical resistivity at 500 °C.

than the active zone volume. Hence, the resistivity is slightly higher for a given resistance, as the model allows for some electrical conductance in the bed space beneath the central electrode. Regardless of the calculation method, the trend is the same; resistivity increases as the particle size decreases. This trend is believed to be due to a larger number of contact points required to bridge the gap between the central and wall electrodes with smaller particles. This is consistent with literature findings from multiple tests on carbon materials in fixed and fluidized beds.[9,21,40] Still, the impact of particle size in fluidized beds may be more complex due to the influence of particle size on hydrodynamics.

D. *Arcing Potential*

Electric arcing occurs when an electrical discharge jumps between conductors, ionizing the gas medium to create a conductive path due to a sufficient voltage difference. The minimum voltage at which a gas medium becomes conductive via arcing is referred to as the breakdown voltage (V_B). V_B is a function of

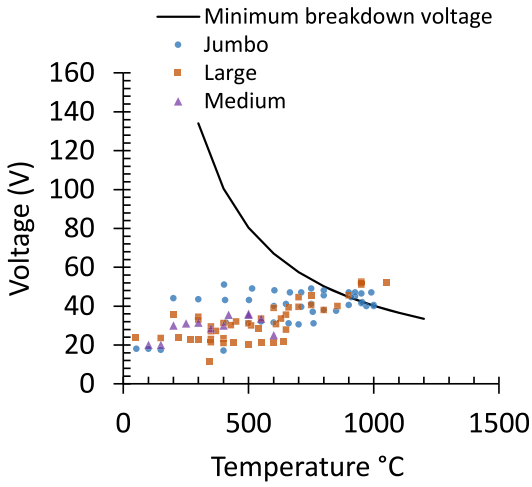

Fig. 10—The experimental voltages applied in this study are compared with the minimum breakdown voltage to form an arc in argon.

temperature. Uhm *et al.* studied the breakdown voltage between concentric cylinders.[41] The experimental results in their study indicate the breakdown voltage of argon decreases with increasing temperature, within the 27 °C to 827 °C range. They indicated that the breakdown voltage at a given temperature, T in kelvins, can be related to a reference breakdown voltage and temperature (V_{BR} at T_R):

$$V_B = \frac{T_R}{T} V_{BR}. \quad [29]$$

In addition to increasing the temperature and voltage, arcing can also be favored by lowering the pressure and conductor gaps, according to Paschen's Law.[42,43] The minimum breakdown voltage of argon at 27 °C is approximately 134 V and approximately 40 V at 1000 °C.[44] The minimum breakdown voltages for argon at temperatures applied in the current study were determined using Eq. [29], with a reference voltage of 134 V at 27 °C, and were plotted in Figure 10. As shown in Figure 10, over 90 pct of data points obtained in the current study applied a potential difference lower than the minimum breakdown voltage curve. Therefore, it can be expected that negligible arcing occurred during most experiments.

E. *Effect of Center Electrode Immersion Depth*

Figure 11 shows the changes in resistance, resistivity-active zone, and resistivity-actual geometry with an ICE of 25, 60, and 95 mm. Resistance generally decreases with an increased ICE. This is likely due to an increase in the bed–electrode contact area as the ICE is increased. If most current passes radially in the active zone and the bed hydrodynamics are not impacted by the ICE, the resistivity is expected to be independent of the ICE. However, a constant resistivity across different ICEs was not observed when the resistivity was calculated assuming that all current goes through the active zone, *i.e.*, applying Eq. [28] (middle graph in Figure 11).

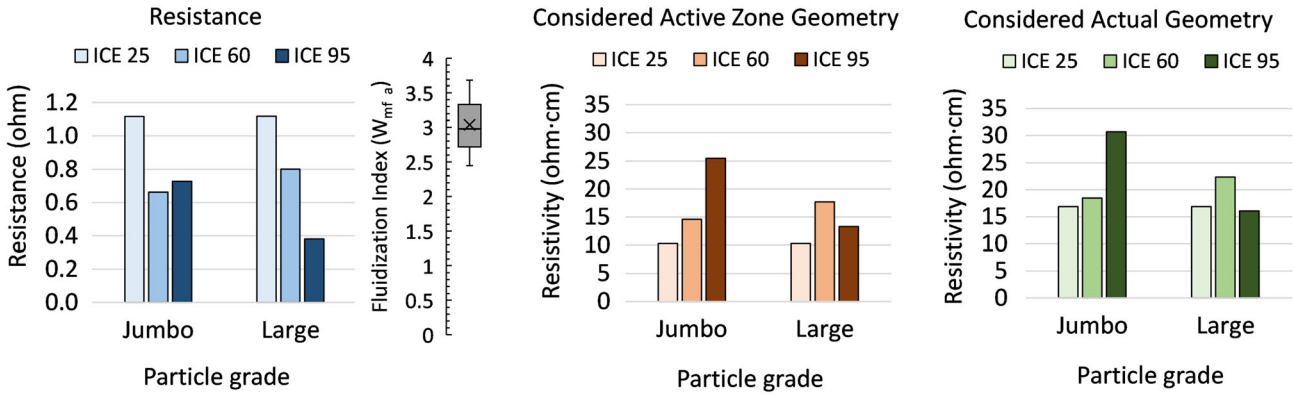

Fig. 11—Electrical resistance (left), resistivity of the active zone assuming all current passes radially through it (middle), and resistivity of the full fluidized bed (right) with jumbo or large graphite flakes at 500 °C.

Using the reactor's inner geometry in COMSOL with the measured potential drops and currents across the fluidized bed, the resistivities of the full fluidized bed (represented by a uniform solid) were calculated (right graph in Figure 11). As the resistivities still vary with ICE, it is believed that the ICE has an impact on bed hydrodynamics and its resulting resistivity.

F. *Model Validation: FDM Model vs Experiment*

Figures 12 and 13 facilitate comparison between the FDM model and experiments, in terms of resistance and power. For many conditions, the model results show good agreement with experimental values. It is believed that the average bed temperature in the experiments may be slightly lower than the measured temperature, since the bed temperature measurement occurred near the bottom of the central electrode, *i.e.*, in the active zone where most of the current passes. The bottom zone, *i.e.*, with relatively less current passing and less Joule heating, may be cooler than the active zone. To substantiate this hypothesis, Figure 14 demonstrates that for a given ICE of 25 mm, the measured temperature decreases when the thermocouple is positioned below the active zone. Hence, some discrepancies between the model results and experimental values were expected, particularly with smaller ICEs. Furthermore, if the bottom zone is cooler than the measured temperature, the actual fluidization index for this zone would be lower than the estimated value, as the lower density gas in the bottom zone would also have a lower velocity. This could have led to poor or no fluidization in the bottom zone, which would not be captured by the model.

G. *Heat Transfer Model Verification*

This study evaluated heat transfer models for the experimental setup using FEM and FDM. Figure 15 compares the power consumption of jumbo particles at different temperatures using FEM, FDM, and experimental methods, assuming either a constant outer wall temperature of 60 °C or one determined by natural convection for an ICE of 95 mm. Power loss depends on the FB temperature, which is influenced by variations in resistivity. These variations may arise from changes in hydrodynamics or particle properties. The FEM model employed the same correlation as the FDM model to evaluate electrical resistivity in the fluidized bed. For a given bed temperature, varying the ICE has no noticeable effect on the predicted power consumption, either with the FEM model or FDM model; therefore, results for only the 95-mm ICE are presented in Figure 15. With an outer wall temperature of 60 °C, FEM and FDM predictions are similar at low temperatures, but diverge as temperature increases above 280 °C. This suggests that the actual geometry, as considered in the FEM model, causes more heat loss that is not captured by the FDM model at higher temperatures.

The FEM model with natural convection is believed to be a more accurate representation of the experimental conditions, as demonstrated in Figure 15. This method shows lower power consumption compared to the FEM model with $T\_wall = 60$ °C, across the temperature range. Natural convection, as a mode of heat transfer, may lead to a lower heat loss as the true wall temperature can be higher than 60 °C.

Figure 16 illustrates the bed's predicted electrical resistance values for various ICE levels at 1000 °C, showing that the FEM model predicts lower resistance compared to the FDM model. This discrepancy arises from differences in geometric assumptions. The FDM model simplifies the geometry and assumes current flows only in the active zone, while the FEM model accounts for a more accurate geometry, including a vertical current flow component, which reduces overall resistance. Greater immersion of the central electrode increases the electrical contact area. This results in lower resistance with an ICE of 95 mm and higher resistance with an ICE of 25 mm.

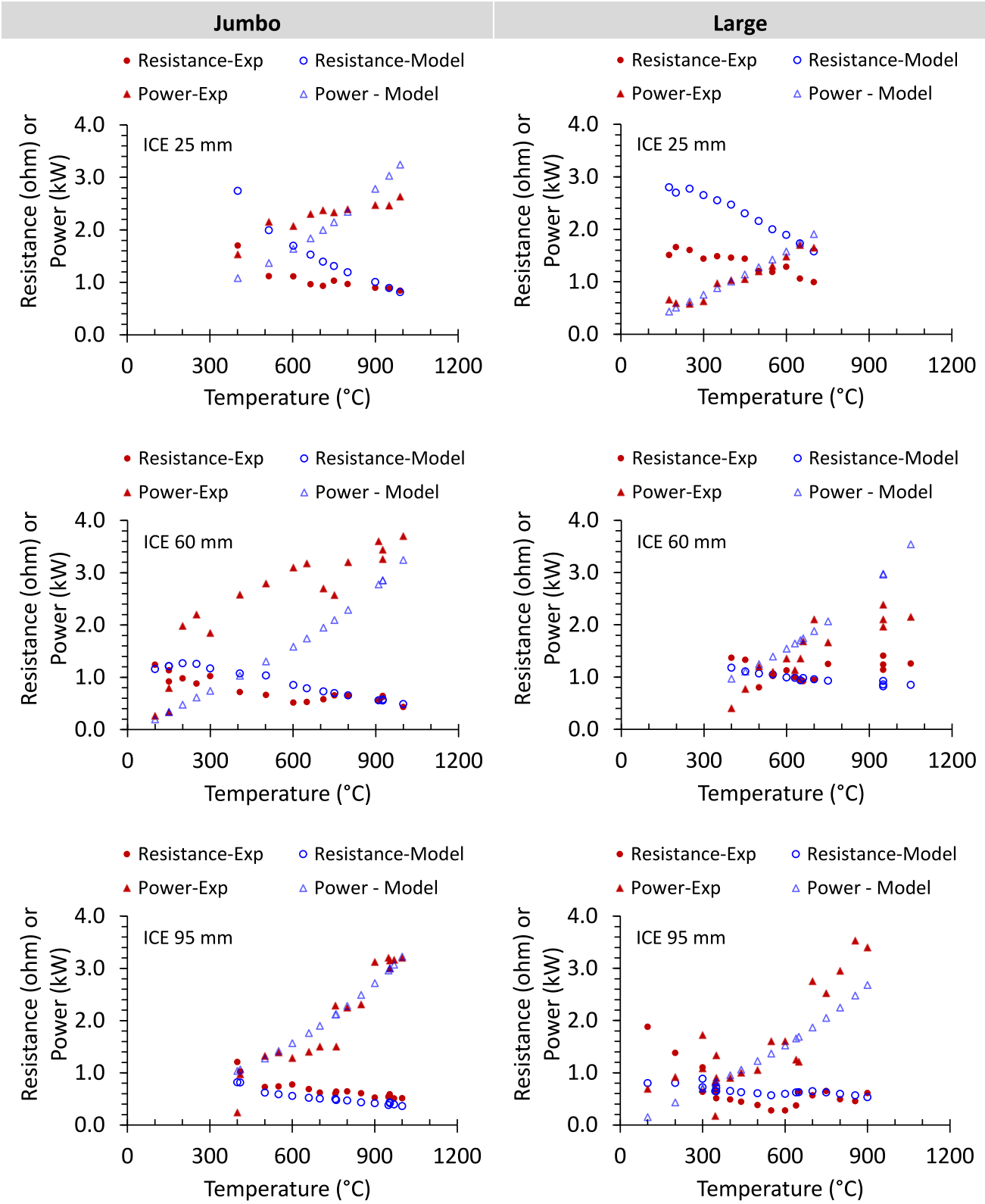

Fig. 12—Experimental and predicted electrical resistance and power for jumbo (column 1) and large (column 2) particle sizes. *Note* in the model, the structural coefficient K is 4 for jumbo and 3 for large.

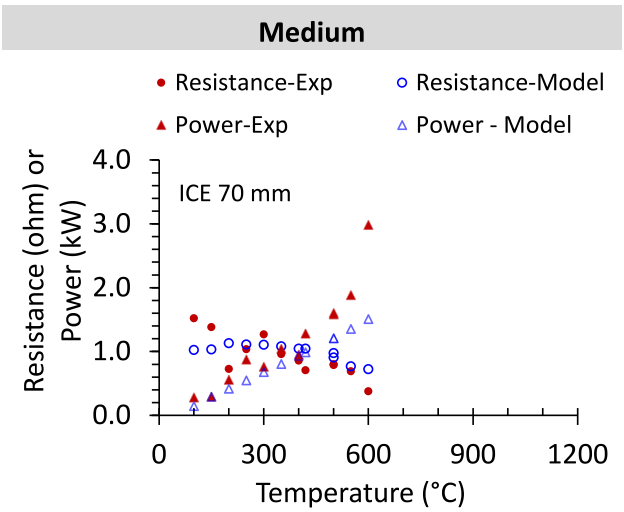

Fig. 13—Experimental and predicted electrical resistance and power for the particle size medium. *Note* in the model, the structural coefficient K is 2 for medium.

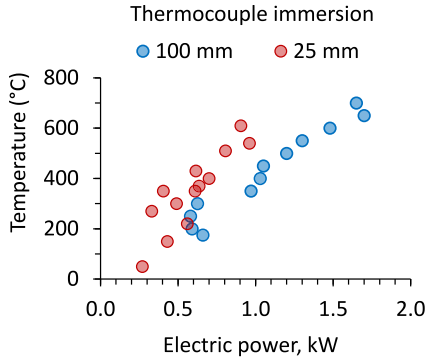

Fig. 14—The temperature of the fluidized bed at two different heights (thermocouple immersion depths of 25 and 100 mm) for large particles with an ICE of 25 mm.

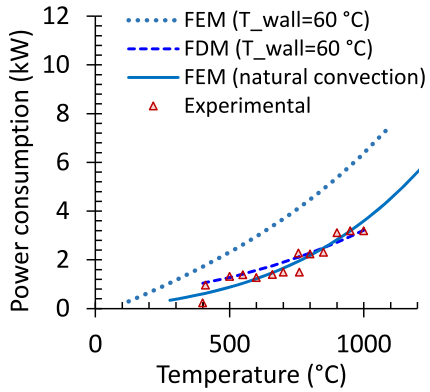

Fig. 15—Power consumption at different temperatures for the comparison of experiments, FEM, and FDM with jumbo particles and an ICE of 95 mm.

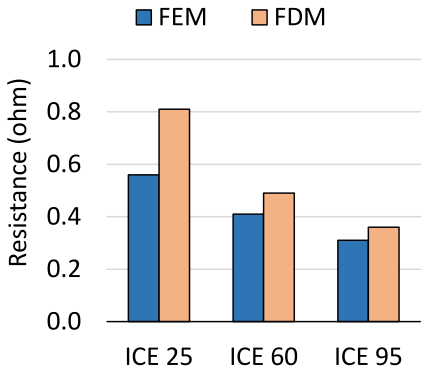

Fig. 16—Resistance for various ICE values at 1000 °C.

VII. CONCLUSION

Three populations of graphite flakes, *i.e.*, jumbo, large, and medium, were processed in a fluidized bed system operating up to 1000 °C. FDM and FEM models were created to simulate the system, accounting for heat transfer and electrical resistivity, with parameters that vary based on fluidization properties.

Overall, the electrical resistance has a decreasing trend as temperature increases from ambient to 1000 °C. One could argue that there is a correlation between graphite's intrinsic resistivity and the fluidized bed resistivity; however, fluidization may be more impactful. Overall, the effect of the complete fluidization index on resistivity is less pronounced when the index is above 1. A bed of smaller particles tends to have a higher electrical resistance compared to a bed of larger particles; this trend is attributed to the greater number of contact points required for smaller particles to bridge the gap between electrodes. The electrical resistivity of fluidized beds could be impacted by arc formation; however, over 90 pct of the experimental data points in this study involved electrical potentials below the estimated minimum breakdown voltage.

The FDM model predicts the electrical resistance of fluidized beds, enabling estimations of steady-state bed temperatures and power consumption. The model is more accurate when the central electrode immersion is greater; lower immersion depths may result in a significant temperature gradient between the active and bottom bed zones in the fluidized bed, which is not properly captured by the FDM model. This implies that the electrode immersion is crucial to ensure a uniform bed temperature.

The FDM model can be used for quick evaluations. However, to improve heat loss predictions, the FEM model accounted for a more detailed geometry. Compared to the FDM model, for a constant wall temperature, the FEM model predicts a higher power consumption at higher bed temperatures (> 500 °C). For instance, at 900 °C, the FEM model predicts 45 pct more power consumption than the FDM model. The FDM model offers a quick and cost-effective evaluation using readily available software. In contrast, the FEM model provides a more accurate consideration of geometry and reactor materials, enabling more effective

reactor design. Both the FDM and FEM models apply fluidized bed parameters to evaluate resistivity. The experimental investigation showed that smaller particles further complicate fluidization, making predictions and operation more difficult. Further research is essential to better characterize the electrical resistivity of fluidized beds and refine models when performance deviates from ideal fluidization.

ACKNOWLEDGMENTS

This work was supported by the Government of Canada, *via* Natural Resources Canada's Critical Minerals RD&D Funding. Nouveau Monde Graphite provided the sample graphite particle populations. The authors thank Professor Mykhailo Hubynskyi and Dr. Tetyana Vvedenska, from Thermal and Material Engineering Center SP. Z O. O., for their support and contributions to the study.

AUTHOR CONTRIBUTIONS

Imtiaz Ahmed contributed toward conceptualization, formal analysis, visualization, writing—original draft, and writing—review and editing. Serhii Fedorov contributed toward methodology, software, validation, investigation, and formal analysis. Artem Sybir: contributed toward resources, methodology, and investigation. Semen Hubynskyi contributed toward investigation and formal analysis. Marc Duchesne contributed toward conceptualization, formal analysis, funding acquisition, project administration, supervision, and writing—review and editing.

CONFLICT OF INTEREST

The author(s) declare that there are no conflicts of interest related to this research, authorship, or publication of this paper.

FUNDING

Open access funding provided by Natural Resources Canada library.

OPEN ACCESS

NOMENCLATURE

SYMBOLS

Ar	Archimedes number
$a_{ef.z}$	Apparent thermal diffusion coefficient of the fluidized bed (FB) in the vertical direction
$a_{ef.r}$	Apparent thermal diffusion coefficient of the FB in the radial direction
C	Sutherland constant
c_m	Specific heat capacity of the fluidized material
C_q	Heat coefficient
d_p	Characteristic particle diameter
D_{CE}	Central electrode (CE) diameter
D_{fc}	Inner diameter of the side wall electrode (SWE)
D_{ts}	Inner diameter of the top space
F_p	Average cross-sectional area of a particle
g	Acceleration due to gravity
H_{AZ}	Height of the active FB zone
H_{bs}	Bed height beneath the CE
H_{fc}	Fluidization chamber height
H_{sb}	Bed height prior to fluidization
H_{ts}	Top space height
I_Σ	Sum of the electric currents through each horizontal layer
I_i	Electric current for the horizontal layer "i"
K	Structure coefficient accounting for the influence of broken contacts between particles in the bed
l_p	Average distance between neighboring particle centers
P	Pressure
$Q_{eli,j}$	Heat released from a computational element at the location (i,j) in the fluidized bed
q_{Bot}	Heat flux through the bottom section of the reactor caused by thermal conductivity
q_G	Heat flux of effluent gases through the top section of the reactor
q_{ML}	Heat flux of the material carried over by the gases including evaporated impurities
q_P	Heat flux of the material moving downward to the discharge port
q_{SWE}	Heat flux through the SWE which is equal to the heat losses through the insulation

q_{Top}	Heat flux through the top section of the reactor caused by radiation and thermal conductivity
q_v	Specific Joule heating rate inside the FB
$R_{c\Sigma i,j}$	Resistance of a contacting pair of particles
$R_{i,j}$	Horizontal resistance of a single-volume element for the current passing from the CE to the SWE
R_c	Inter-particle electrical contact resistance
$R_c\prime$	Corrected electrical contact resistance
R_p	Electrical resistance of a single particle
Re_{mf}	Reynolds number at the minimum fluidization velocity
r, z	Radial and vertical coordinates, respectively
s_p	Thickness of a particle
T_wall	Reactor wall temperature
T	Temperature of the fluidized bed
T_R	Reference temperature for the breakdown voltage
U^*	Voltage on the central electrode surfaces
u_{cf}	Complete fluidization velocity
u_{mf}	Minimum fluidization velocity
$V_{eli,j}$	Volume of an element, where i and j refer to the location of the element
V_{bubble}	Volume of bubbles in the fluidized bed
V_B	Electric breakdown voltage for arc formation
V_{BR}	Reference breakdown voltage at temperature T_R
V_{fb}	Volume of the fluidized bed
W_{cf_a}	Active zone fluidization index as a ratio of the active zone superficial gas velocity to the complete fluidization velocity
W_{cf_b}	Bottom zone fluidization index as a ratio of the bottom zone superficial gas velocity to the complete fluidization velocity
W_{mf_a}	Fluidization index as a ratio of the active zone superficial gas velocity to the minimum fluidization velocity

GREEK LETTERS

ρ_g	Density of the gas medium
ρ_m	Density of the fluidized material
ν	Kinematic viscosity of the gas
μ_0	Gas dynamic viscosity at standard conditions ($T_0 = 293$K and $P_0 = 101{,}325$Pa)
μ	Gas dynamic viscosity
ε	FB void fraction
ε_{mf}	FB void fraction at the minimum fluidization condition
φ_b	Bubble fraction in the FB
$\Omega_{i,j}$	Resistivity of a computational volume element
Ω	Average electrical resistivity of the FB active zone
ΔU	Electrical potential drop
$\sum R_j$	Overall resistance of a single horizontal layer of the FB
λ_{ef}	FB Effective thermal conductivity

ACRONYMS

AC	Alternating current
BCs	Boundary conditions
CE	Central electrode
DC	Direct current
EHFB	Electrically heated fluidized bed
FB	Fluidized bed
FDM	Finite Difference Method
FEM	Finite Element Method
ICE	Immersion depth of the central electrode in a static fluidized bed
SWE	Side wall electrode
TRL	Technology readiness level
VBA	Visual Basic for Applications

REFERENCES

1. IEA: *Graphite—Analysis*, IEA. https://www.iea.org/reports/graphite. Accessed 16 Dec 2024.
2. P. Barrera: Graphite Supply Needs to Increase Nearly 500 Percent by 2050. https://investingnews.com/daily/resource-investing/battery-metals-investing/graphite-investing/graphite-supply-needs-increase/. Accessed 30 Nov 2020.
3. Homeostasis Whitepaper: CO_2 into critical materials. https://homeostasis-earth.notion.site/Homeostasis-Whitepaper-8fc9369896df47f88efdeb09bcc7ee75. Accessed 10 Dec 2024.
4. K. Shen, X. Chen, W. Shen, Z.-H. Huang, B. Liu, and F. Kang: *Carbon*, 2021, vol. 173, pp. 769–81.
5. G.R.A. Kumara, H.M.G.T.A. Pitawala, B. Karunarathne, M.M.M.G.P.G. Mantilaka, R.M.G. Rajapakse, H.-H. Huang, K.K.H. De Silva, and M. Yoshimura: *Sci. Rep.*, 2021, vol. 11, p. 22713.
6. A.D. Jara, A. Betemariam, G. Woldetinsae, and J.Y. Kim: *Int. J. Min. Sci. Technol.*, 2019, vol. 29, pp. 671–89.
7. S. Chehreh Chelgani, M. Rudolph, R. Kratzsch, D. Sandmann, and J. Gutzmer: *Miner. Process. Extr. Metall. Rev.*, 2016, vol. 37, pp. 58–68.
8. World Intellectual Property Organization, WO2005028978A1, 2005.
9. V.A. Borodulya, S.S. Zabrodsky, and A.I. Zheltov: *AIChE Symp. Ser.*, 1973, vol. 69, pp. 106–14.
10. W. Graham and E.A. Harvey: *Can. J. Chem. Eng.*, 1966, vol. 44, pp. 17–19.
11. F. Jiang, Y. Yao, B. Natarajan, C. Yang, T. Gao, H. Xie, Y. Wang, L. Xu, Y. Chen, J. Gilman, L. Cui, and L. Hu: *Carbon*, 2019, vol. 144, pp. 241–48.
12. P. Ouzilleau, A.E. Gheribi, P. Chartrand, G. Soucy, and M. Monthioux: *Carbon*, 2019, vol. 149, pp. 419–35.
13. A. Sybir, M. Hubynskyi, S. Fedorov, S. Hubynskyi, T. Vvedenska, and V. Bezuglyi: *Min. Miner. Depos.*, 2020, vol. 14, pp. 43–49.
14. W.A. Smith: Method of Heating Carbon. Patent US1004923, 1911.
15. S.S. Fedorov, U. Singh Rohatgi, I.V. Barsukov, M.V. Gubynskyi, M.G. Barsukov, B.S. Wells, M.V. Livitan, and O.G. Gogotsi: *J. Fluids Eng.*, 2016, vol. 138, p. 044502.
16. I. Ahmed, M. Duchesne, Y. Tan, and D.Y. Lu: *Ind. Eng. Chem. Res.*, 2024, vol. 63, pp. 4205–35.
17. T.M. Knowlton: PhD Dissertation, Iowa State University, 1971.
18. P.A. Eidem, M. Tangstad, and J.A. Bakken: *Metall. Mater. Trans. B*, 2008, vol. 39B, pp. 7–15.
19. G. Rouget, B. Majidi, D. Picard, G. Gauvin, D. Ziegler, J. Mashreghi, and H. Alamdari: *Metall. Mater. Trans. B*, 2017, vol. 48B, pp. 2543–50.
20. A. Bernard, N. Khalil, I. Ahmed, D. McCalden, J. Haelssig, A. Macchi, and M. Duchesne: *Powder Technol.*, 2024, vol. 431, p. 119097.

21. I. Ahmed, Y. Tan, and M. Duchesne: in *Proceedings of the 62nd Conference of Metallurgists*, Toronto, Canada, Springer, 2023.
22. M.E. Aérov and O.M. Todes: *Hydraulic and Thermal Principles of Operation of Devices with a Stationary and Fluidized Granular Bed (Гидравлические и Тепловые Основы Работы Аппаратов Со Стационарным и Кипящим Зернистым Слоем)*, Publishing House "Chemistry," Moscow, 1968.
23. F.M. White and J. Majdalani: *Viscous Fluid Flow*, 4th ed. McGraw Hill, LLC, New York, 2022.
24. M.L. Huber and A.H. Harvey: Viscosity of Gases. https://tsapps.nist.gov/publication/get_pdf.cfm?pub_id=907539.
25. F. Miró Miró and F. Pinna: *J. Fluid Mech.*, 2020, vol. 890, p. R4.
26. N.I. Gelperin, V.G. Einstein, and V.B. Kvash: *Fundamentals of Fluidization Engineering (Основы Техники Псевдоожижения)*, Publishing House "Chemistry," Moscow, 1967.
27. S.S. Fedorov, M.V. Hubynskyi, S.M. Foris, and D.S. Dvoretsky: *Analysis of Carbon Material Mixing Processes in Electrothermal Fluidized Bed Furnaces (АНАЛИЗ ПРОЦЕССОВ ПЕРЕМЕШИВАНИЯ УГЛЕРОДНОГО МАТЕРИАЛА В ЭЛЕКТРОТЕРМИЧЕСКИХ ПЕЧАХ КИПЯЩЕГО СЛОЯ)*, vol. 5, Metallurgical Heat Engineering, 2013, pp. 155–67.
28. S.S. Fedorov, V.A. Bezugly, M.V. Hubynskyi, and V.E. Kremneva: *Metall. Min. Ind.*, 2015, vol. 6, pp. 116–21.
29. M. Gubinskyi, S. Fiodorov, Y. Kremniova, O. Gogotsi, and T. Vvedenska: *Power Engineering and Information Technologies in Technical Objects Control*, CRC Press, Boca Raton, 2016, pp. 173–80.
30. S.S. Fedorov, M.V. Gubinskii, and S.N. Foris: *J. Eng. Phys. Thermophys.*, 2016, vol. 89, pp. 627–35.
31. V.A. Borodulya: *High-Temperature Processes in Electrothermal Fluidized Bed (Высокотемпературные процессы в электротермическом кипящем слое)*, Science and Technology (Наука и техника), Minsk, 1973.
32. S. Fedorov: PhD Dissertation, Ukrainian State University of Science and Technologies, 2018.
33. S. Jiang, T.J. Horn, and V.K. Dhir: *Int. J. Thermophys.*, 2000, vol. 21, pp. 941–63.
34. F. Bendjebbar, P. Andre, M. Benbakkar, D. Rochette, S. Flazi, and D. Vacher: *Plasma Sci. Technol.*, 2012, vol. 14, pp. 683–92.
35. L. Gallais, T. Vidal, E. Lescoute, Y. Pontillon, and J.L. Rullier: *J. Appl. Phys.*, 2021, vol. 129, p. 043102.
36. COMSOL Documentation. https://doc.comsol.com/6.2/docserver/#!/com.comsol.help.comsol/helpdesk/helpdesk.html. Accessed 19 March 2024.
37. C. Paraskevoulakos, B. Roebuck, K.R. Hallam, and P.E.J. Flewitt: *SN Appl. Sci.*, 2022, vol. 5, p. 28.
38. M. Okada, N. Ohta, O. Yoshimoto, M. Tatsumi, and M. Inagaki: *Carbon*, 2017, vol. 116, pp. 737–43.
39. W.M. Goldberger and A.K. Reed: *Chem. Eng. Prog. Sympos. Ser.*, 1966, vol. 62, pp. 71–75.
40. W. Graham and E.A. Harvey: *Can. J. Chem. Eng.*, 1965, vol. 43, pp. 146–49.
41. H.S. Uhm, S.J. Jung, and H.S. Kim: *J. Korean Phys. Soc.*, 2003, vol. 42, pp. S989-93.
42. Y. Fu, P. Zhang, J.P. Verboncoeur, and X. Wang: *Plasma Res. Express*, 2020, vol. 2, p. 013001.
43. E. Husain and R. Nema: *IEEE Trans. Electr. Insul.*, 1982. https://doi.org/10.1109/TEI.1982.298506.
44. R. Massarczyk, P. Chu, S.R. Elliott, K. Rielage, C. Dugger, and W. Xu: *J. Instrum.*, 2017, vol. 12, p. P06019. https://doi.org/10.1088/1748-0221/12/06/P06019.